HHS Public Access

Author manuscript

Sci Transl Med. Author manuscript; available in PMC 2020 July 13.

Published in final edited form as:

Sci Transl Med. 2020 March 25; 12(536): . doi:10.1126/scitranslmed.aaw3210.

An ocular glymphatic clearance system removes β-amyloid from the rodent eye

Xiaowei Wang[1,2], **Nanhong Lou**[2], **Allison Eberhardt**[2], **Yujia Yang**[3], **Peter Kusk**[1], **Qiwu Xu**[2], **Benjamin Förstera**[4,5], **Sisi Peng**[2], **Meng Shi**[3], **Antonio Ladrón-de-Guevara**[2], **Christine Delle**[1], **Björn Sigurdsson**[1], **Anna L. R. Xavier**[1], **Ali Ertürk**[4,5], **Richard T. Libby**[6], **Lu Chen**[3,*], **Alexander S. Thrane**[1,7], **Maiken Nedergaard**[1,2,*]

[1]Center for Translational Neuromedicine, Faculty of Medical and Health Sciences, University of Copenhagen, Denmark, Blegdamsvej 3B, 2200 Copenhagen N

[2]Center for Translational Neuromedicine, University of Rochester Medical School, Elmwood Avenue 601, Rochester, NY 14642, USA

[3]Center for Eye Disease and Development, Vision Science Graduate Program, and School of Optometry, University of California Berkeley, Berkeley, CA 94720, USA

[4]Institute for Stroke and Dementia Research, Klinikum der Universität München, Ludwig Maximilians University of Munich (LMU), 81377 Munich, Germany

[5]Institute for Tissue Engineering and Regenerative Medicine (iTERM), Helmholtz Center München, 85764 Munich, Germany

[6]Department of Ophthalmology, University of Rochester Medical Center, Rochester, NY, 14642, USA

[7]Department of Ophthalmology, Haukeland University Hospital, Jonas Lies Vei 65, 5021 Bergen, Norway

Abstract

Despite high metabolic activity, the retina and optic nerve head lack traditional lymphatic drainage. We here identified an ocular glymphatic clearance route for fluid and wastes via the proximal optic nerve in rodents. B-amyloid (Aβ) was cleared from the retina and vitreous via a pathway dependent on glial water channel aquaporin-4 (AQP4) and driven by the ocular-cranial pressure difference. After traversing the lamina barrier, intra-axonal Aβ was cleared via the perivenous space and subsequently drained to lymphatic vessels. Light-induced pupil constriction

[*]**Correspondence should be addressed to:** Dr. Maiken Nedergaard, Center for Translational Neuromedicine, Faculty of Medical and Health Sciences, University of Copenhagen, Denmark, Blegdamsvej 3B, 2200 Copenhagen N, Denmark. nedergaard@sund.ku.dk; Dr. Lu Chen, Center for Eye Disease and Development, Vision Science Graduate Program, and School of Optometry, University of California Berkeley, Berkeley, California, United States. chenlu@berkeley.edu.

Author contributions: M.N. and L.C. supervised research. X.W., N.L., A.S.T. and M.N. designed the experiments, performed the data analysis, prepared the figures and wrote the manuscript. B.F. and X.W. performed uDISCO experiments. Q.X. performed TMA^{+} recordings. X.W. and P.K.J. performed pupillometry. X.W., A.E., Y.Y., N.L. performed IOP recordings. X.W., N.L., A.E., Y.Y., A.L., Q.X., S.P., A.L.R.X.,C.D., B.S. performed the remainder of imaging and data collection. X.W., L.C., Y.Y., M.S., N.L., and R.T.L. generated murine models. Data needed to evaluate the conclusion is presented in this manuscript or supplementary material.

Competing interests: The authors declare no competing interests.

Data and materials availability: All data associated with this study are present in the paper or the Supplementary Materials.

enhanced efflux, whereas atropine or raising intracranial pressure blocked efflux. In two distinct murine models of glaucoma, Aβ leaked from the eye via defects in the lamina barrier instead of directional axonal efflux. The results suggest that, in rodents, the removal of fluid and metabolites from the intraocular space occurs through a glymphatic pathway that might be impaired in glaucoma.

One Sentence Summary:

Glymphatic pathway clears retinal β- amyloid in rodent via optic nerve and is impaired in glaucoma.

Introduction

Similar to the brain inside the cranial vault, the internal structures of the eye are contained within a confined space, necessitating tight control of fluid homeostasis. Yet, both the eye and the brain are largely devoid of traditional lymphatic vessels, which are critical for the clearance of fluid and solutes from peripheral tissues (1, 2). Recent discoveries have shown that the brain has a quasi-lymphatic system, termed the glymphatic system (3), and traditional lymphatic vessels are also present in the dura mater, one of three layers of fibrous membranes lining the brain's exterior surface (4–6). Neuroimaging studies have recently documented the existence of a glymphatic/lymphatic system in the human brain with drainage to cervical lymph nodes (7–11). Glymphatic/lymphatic transport contributes to clearance of β-amyloid (Aβ), a derivative of amyloid precursor protein (APP) that is a main constituent of amyloid plaques in the brain (12) and likewise of amyloid deposits in the retina (13). Extracellular Aβ and tau are regulated by the sleep-wake cycle (14, 15), possibly reflecting increased production during neural activity (16) and/or enhanced clearance during sleep (17). Several authors suggested the existence of an ocular glymphatic system based on clinical observations and the identification of missing pieces of how the neuroretina tightly controls volume homeostasis (18–21). Experimental data supports this concept by demonstrating retrograde cerebrospinal fluid (CSF) transport along the perivascular spaces in the optic nerve (22) and more recently an impairment of retrograde transport in glaucoma (23). However, the primary function of glymphatic transport is clearance of metabolic waste. In the eye, it is the highly active retinal neurons that are producing waste products and therefore in need of a clearance system. We here determined whether the optic nerve might serve as a pathway for efflux of ocular fluid and thereby supporting clearance of waste products from the retina.

Results

Tracer imaging supports the existence of an ocular glymphatic clearance system

Because the electrically active neural tissues of the retina produce Aβ (3, 24) and other potentially neurotoxic protein cleavage products such as tau (25), we explicitly sought evidence of an intraocular anterograde glymphatic/lymphatic clearance system in mice. First, we injected HiLyte-594-tagged human β-amyloid (hAβ) into the vitreous body of mice and visualized tracer distribution one hour later. Then we used ultimate three-dimensional(3D) imaging of solvent-cleared organs (uDISCO) whole-body clearing (26) to

analyze the eye and tracer in transparent mouse heads. 3D reconstruction of light-sheet microscopy data suggested that in addition to anterior routes, hAβ tracer exited the eye along the optic nerve (Fig. 1A, fig. S1A). Transport along the optic nerve also occurred after noninvasive intravascular delivery of either the radiolabeled K^+-analog ($^{86}Rb^+$) or fluorescein isothiocyanate (FITC)-cadaverine, a tracer that permeates the blood-retinal barrier (BRB) but not the bloodbrain barrier (27) (fig. S1B–D). Whole-mount preparation of the optic nerve confirmed that hAβ tracer is transported anterograde along the nerve (Fig. 1B). Moreover, use of reporter mice in which arteries and arterioles are identified by DsRed expression in mural cells (28) revealed that hAβ tracer preferentially accumulated in the perivascular space along the optic nerve veins rather than along arterioles (Fig. 1C). In contrast to hAβ tracer, Alexa Fluor (AF)-dextran (3, 10, and 500 kDa) did not enter the nerve after intravitreal administration (Fig. 1D, fig. S1E). After suprachoroidal delivery, tracer was also transported along the optic nerve (fig. S1F). The injection of trace amounts of hAβ tracer was not associated with retinal cytokine release, glial activation, apoptosis, or alteration in BRB permeability (fig. S2A–G, table S2). Sectioning and high-resolution imaging of the eye showed that, in addition to perivenous accumulation, hAβ tracer was taken up by retinal ganglion cells (RGCs, RNA-binding protein with multiple splicing-positive) as well as amacrine cells (AP-2α$^+$) (fig. S3A–E) and transported along neuron-specific class III β-tubulin (TUJ1)-positive axons, consistent with rapid neuronal uptake of hAβ (29) (Fig. 1E–F). In the optic nerve, glial cells of the oligodendrocytic (OLIG2$^+$) and astrocytic (GLT-1$^+$) lineages also exhibited sparse hAβ tracer uptake (fig. S3E–I). The hAβ tracer accumulation peaked at 274 ± 20 μm from the optic nerve head (ONH) and tapered off gradually in the distal nerve (table S1), suggesting hAβ tracer exit the nerve anterior to the optic chiasm. This notion was supported by the observation that the dural sheath surrounding the proximal segment of the optic nerve densely accumulated tracer (Fig. 1E, fig.S3J). Additional analysis revealed traditional lymphatic vessels embedded in the dural sheath and surrounding loose tissue (30–32) (fig. S3K–M). These vessels did not contain red blood cells or stain with intravascularly-delivered lectin, but they labeled positive for the conventional lymphatic markers, lymphatic vessel endothelial hyaluronan receptor 1 (LYVE1), vascular endothelial growth factor receptor 3 (VEGFR3), Prospero homeobox protein 1(*Prox1*), and podoplanin (PDPN) (2, 5). In support of this, hAβ had accumulated in the ipsilateral cervical lymph nodes in animals examined three hours after intravitreal injection (33) (Fig. 1G). Imaging after dual injections of hAβ tracer in the vitreous body in conjunction with a tracer in the cisterna magna (CM) highlighted tracer transport within the optic nerve in both anterograde and retrograde directions with limited spatial overlap (Fig. 1H–I). As previously reported, tracers injected in the CM were transported along perivascular spaces in the optic nerve (22). Use of NG2-DsRed-expressing reporter mice revealed CM-injected tracers were predominantly transported along the periarterial and pericapillary spaces (Fig. 1J–K, fig. S3N), in contrast to the intravitreal tracers, which accumulated along the veins (Fig. 1C). Collectively, these observations show hAβ is transported by axons and along the perivenous space in the optic nerve after intravitreal delivery. From there, hAβ exits the nerve via dural lymph vessels located in the outer (dural) layer of meninges lining the optic nerve and orbital lymphatics (fig. S3J–L) consistent with recent reports about lymphatic CSF drainage. Anterior lymphatic drainage pathways may have also contributed to the clearance of hAβ described in our study (2, 34).

Ocular Aβ clearance is affected by glial water channel AQP4

Astroglial expression of water channel AQP4 on end feet plastering nearly the entire brain vasculature has been shown to facilitate cerebral clearance of amyloid-β (3, 17, 35, 36). Because retinal Müller glia express abundant AQP4, we next asked whether glial AQP4 facilitates Aβ clearance from the retina and along the optic nerve. We performed intravitreal injection of fluorescently tagged hAβ as described above and compared tracer movement in *Aqp4*$^{-/-}$ and *Aqp4*$^{+/+}$ mice. Baseline intraocular pressure (IOP) was comparable for *Aqp4*$^{-/-}$ and wildtype mice (Fig. 2A). *Aqp4* deletion was associated with a significantly reduced retinal hAβ penetration ($p < 0.05$, Fig. 2B–C). Similarly, *Aqp4* deletion caused a significant reduction in the clearance of hAβ movement along the nerve ($P < 0.05$, Fig. 2D–G). These data demonstrate that ocular glymphatic clearance is facilitated by AQP4 expression in retinal Müller glia and pre-laminar astrocytes.

Translaminar pressure difference drives ocular clearance

Pressure difference is a principal driving force of directional fluid transport. Because IOP under physiological conditions exceeds intracranial pressure (ICP), it is possible that the pressure difference across the lamina cribrosa contributes to fluid flow along the optic nerve (37). To define the role of the Translaminar pressure difference (TPD) in transport of hAβ tracer, we manipulated ICP by either withdrawal or infusion of artificial CSF (aCSF) in the CM while monitoring ICP. ICP manipulation with these methods was not associated with IOP alteration (38) (Fig. 3A). Decreasing ICP from baseline (3.6 ± 0.4 mmHg) to 0.5 ± 0.2 mmHg was associated with a sharp increase in the total hAβ tracer signal and peak intensity of hAβ tracer transport in the proximal optic nerve 30 min after intravitreal injection (Fig. 3B–E). Conversely, increasing ICP to 16.7 ± 0.6 mmHg (Fig. 3A) significantly decreased hAβ tracer clearance into the optic nerve ($p < 0.001$, Fig. 3B–E). Combined, these data show that hAβ tracer transport along the nerve is reduced when TPD is decreased and is increased when TPD is elevated.

Light-induced pupil constriction increases ocular glymphatic clearance

Prior observations have shown that repeated constriction of the pupil and ciliary body during accommodation enhances aqueous outflow in healthy human subjects, hypothesized to be via trabecular and uveoscleral routes (39, 40). We next asked whether transport of hAβ along the optic nerve is influenced by physiological pupil constriction *in vivo*. To address this question, we compared transport of hAβ tracer in mice stimulated with light at 1 Hz to control mice kept in darkness. A subset of mice exposed to stimulation received atropine (1%, eye drops) to block the light-induced pupillary constriction reflex, and another subset of mice received pilocarpine (2%, eye drops) to achieve static constriction without light stimulation (Fig. 4A). The analysis showed that light stimulation increased hAβ transport in the optic nerve. The total hAβ tracer signal, peak intensity, and distance of transport were all sharply increased by light stimulation at 30 min after hAβ administration (Fig. 4B–D; the findings were reproduced in rats: fig. S4A–E, and not influenced by varying the injection rate or volume: fig. S4F). Tracer accumulation in mice kept in darkness increased slowly and reached the same amplitude as that in the light-stimulated ones at 2 hours after intravitreal injection of hAβ tracer (fig. S5A–I). Infrared pupillometry confirmed that light stimulation

induced alternating constriction and dilation of the pupil, detected as high variance in pupil size. In contrast, animals kept in darkness, as well as light-stimulated animals pretreated with atropine, exhibited essentially no pupil movement (Fig. 4E–G). Atropine completely blocked light-induced pupil constriction, as well as the light-related acceleration of hAβ tracer transport (Fig. 4B–G), whereas pilocarpine-induced tonic pupillary constriction did not appear to affect transport (Fig. 4B–D). Rebound and intracameral tonometry failed to demonstrate a consistent effect of repeated light stimulation and pupillary constriction on IOP in the short time scale of our experiment (fig. S5J–L), although vitreous pressure transients have been previously demonstrated in larger animals (primates) during ciliary body contraction (41). Intravitreal hAβ tracer was not transported postmortem (Fig. 4B, fig. S5B, F, table S1), indicating that passive diffusion did not contributes to hAβ tracer dispersion along the optic nerve. These data suggest repeated pupil and potentially ciliary body constriction propels intraocular fluid dispersion along the optic nerve, resulting in enhanced hAβ tracer transport. Combining light stimulation with manipulations of ICP did not change net hAβ tracer transport compared with either low or high ICP alone (fig. S6A–E). Thus, sufficiently large pressure changes can override the effect of natural light stimulation. Conversely, dextran transport was not affected by transiently increasing TPD (fig. S6F).

Lamina barrier defects lead to excessive and pathological glymphatic outflow in glaucoma

Glaucoma is a group of diseases characterized by progressive and irreversible injury to the ONH and RGC degeneration, leading to blindness (42). Increased IOP is a leading risk factor for glaucoma. Our present observations raised the question of whether glaucoma is linked to pathological changes in ocular glymphatic solute transport. To test this, we undertook tracer studies in two distinct murine models of glaucoma and chronic ocular hypertension based on two separate mouse strains (Fig. 5A–K, fig. S7A–G, fig. S8A–L). DBA/2J mice develop a depigmenting iris disease that leads to age-related ocular hypertension (43) (Fig. 5A). Chronic IOP elevation results in significant RGC loss and glaucomatous optic nerve degeneration in most of aged eyes from DBA/2J mice (44) ($p < 0.01$, fig. S7D). Rectifying their IOP with pharmacological, genetic, or surgical interventions has been shown to ameliorate RGC death (45). The chronic circumlimbal suture (CLS) model uses oculopression to reduce aqueous drainage, and thus increase IOP to 28 ± 1.6mmHg (vs. 15 ± 0.4mmHg in controls) in nonpigmented CD-1 mice. This model has also been shown to cause RGC loss (46). Our analysis of young DBA/2J mice showed neither IOP nor hAβ tracer transport along the optic nerve differed from that in the DBA/2J-*Gpnmb*$^{+}$/SjJ (D2-control) mice, a genetically-matched control strain that does not develop ocular hypertension (Fig. 5A–D, table S3). About 50% of DBA/2J mice are severely affected by glaucoma at 11 months, but IOP is usually normalized or only mildly elevated at this stage of the disease and thus less likely to directly influence tracer outflow (44). Using whole-mounts of optic nerve, we found that hAβ tracer transport was sharply increased in an equivalent subset of 11-month-old DBA/2J mice (Fig. 5A–D, fig. S8D), with total hAβ tracer signal significantly increased in 11-month-old DBA/2J mice compared with age-matched D2-control mice ($p < 0.05$, Fig. 5B–D, fig. S8C–D). Similarly, we found that CD-1 CLS, but not sham control mice, exhibited significantly increased hAβ tracer transport one month after surgery, when IOP had normalized (46) (Fig. 5B–D, fig. S8D). High-resolution

confocal imaging of 11-month-old DBA/2J optic nerves revealed hAβ tracer was located primarily in the perivascular space, or outside the RGC axons, as opposed to the intra-axonal distribution noted in young DBA/2J mice and age-matched controls (fig. S7A). This prompted us to determine whether the glial lamina normally acts as a high-resistance barrier that hinders transport of macromolecules. If so, then a corollary of this proposition would be that a failure of the lamina barrier might be a hallmark of glaucoma in these mouse models (47, 48). To test this dual hypothesis, we assessed the passage of increasing molecular sizes of AF-dextran across the lamina after intravitreal injection in D2-control and DBA/2J mice (3, 10, 500 kDa), as well as CLS and sham control CD-1 mice (500 kDa) (fig.S8F–L). We found that dextrans as small as hAβ (3kDa vs. 4.3kDa) failed to pass the glial lamina in mice without glaucoma, despite a transient increase in TPD (fig. 5E–H, fig.S6F, fig. S8). In contrast, we saw dispersion of dextran in 11-month-old DBA/2J and CLS mice, with tracer detectable several millimeters distal to the lamina (Fig. 5E–H, fig. S8B–L). Confocal imaging confirmed that the dextrans were present in the perivascular space or outside the few remaining axons in 11-month-old DBA/2J mice (fig. S7B–C, fig. S8B). These observations suggest that the lamina barrier in the healthy eye diverts extracellular fluid into the axonal compartment at the ONH and thus facilitates directional axonal fluid transport. Although our data do not aim to address the proximal cause of lamina barrier failure, they show that openings in the barrier divert flow of the ocular fluid in the optic nerve from the axonal to the extracellular compartment. Ultrastructural analysis revealed large defects in the glial barrier in old DBA/2J mice, as previously reported (47, 49, 50) (Fig. 5I, fig. S7E). We also tested the alternative hypothesis of axonal loss in old DBA/2J mice causing a general expansion of the extracellular space volume fraction (51). Such an increase in extracellular space of the optic nerve would be expected to facilitate pressure-driven hAβ transport. However, real-time tetramethylammonium (TMA^+) iontophoresis analysis failed to confirm this hypothesis; the mean volume fraction (α) was ~10% of the total volume and did not differ between D2-control mice and DBA/2J mice. The tortuosity factor (λ) was not affected ted in old DBA/2J, (Fig. 5J).

Discussion

Traditionally, the trabecular and uveoscleral outflow routes are considered the two main pathways for efflux of ocular fluid (52). We here suggest the existence of an additional clearance route, present in the eyes of both mice and rats. Efflux via this pathway is facilitated by glial water channel AQP4 and driven by the TPD and light-induced pupil constriction, two important physiological factors associated with normal eye function. Using two distinct murine models, we show an excessive and pathological alteration in glymphatic outflow in glaucomatous eyes. The discovery of this fluid efflux route prompts a re-examination of ocular fluid dynamics and may open up new avenues for treatment of sight-threatening conditions, most notably glaucoma (53).

The existence of the efflux system described here raises several important questions that need to be addressed in future works. For example, is the ocular glymphatic system the principal clearance route for protein metabolites such as Aβ produced by RGCs and other retinal cells? Are any subtypes of RGCs more important for the transport than others? We observed that light stimulation accelerated ocular glymphatic clearance by nearly two-fold.

This increase was eliminated when the pupillary light reflex was pharmacologically blocked with atropine or pupil constriction was pharmacologically induced with pilocarpine, in contrast to the well-known effect of these drugs on the conventional outflow (54). We hypothesize that light-induced pupil movement propels the clearance of retinal metabolic wastes, which raises further questions such as, does solute elimination by this pathway occur preferentially during daytime visual activity, driven by pupil constriction and accommodation, and would this explain why aging and diseases affecting the iris/pupil/ciliary body are so closely linked to glaucoma (55, 56)?

Most descriptions of ocular fluid homeostasis to date focus on the anterior eye, away from the highly metabolically active retina. However, it is perhaps not unexpected that an ocular glymphatic system for waste export from the posterior eye might exist, and an ocular glymphatic system has been predicted by several experienced investigators: In 2015, the Denniston and Wostyn laboratories independently published hypothesis-driven reports (18, 21), providing key arguments for the necessity of a glymphatic system in the eye. As visualized by ultrahigh-resolution adaptive optics, the human retinal vasculature is surrounded by perivascular spaces (18). Postmortem administration of India ink into the subarachnoid space resulted in its accumulation in perivascular spaces of the optic nerve and in collagen fiber bundles that are continuous with the perivascular spaces and radiate out to separate the white matter bundles (57, 58). It was also speculated that Aβ could be cleared from the retina by perivascular transport, and pathological changes in IOP might interfere with glymphatic flow and trigger neurotoxicity by Aβ accumulation (21). Similarly, glymphatic dysregulation due to microgravity could contribute to optic disc edema in astronauts (59, 60). The Yucel laboratory recently provided experimental evidence of a perivascular transport system in the optic nerve after intracisternal tracer administration in live mice (22, 23). We here confirmed and extended these reports by showing that CSF tracer influx occurs along the periarterial and pericapillary spaces in the optic nerve. The focus of our report is, however, transport of tracers in the other direction, from the retina to the CSF. We speculated that fluid transport in this direction would facilitate export of waste products from the metabolically-active retina. Our analysis not only confirmed the hypothesis-driven reports discussed above, but also demonstrates that the ocular clearance path described here differs in important ways from the initial predictions of ocular glymphatic system. We would argue that the best way of addressing the unique features of the ocular glymphatic system might be to compare them to the brain glymphatic system: The ocular and brain glymphatic fluid transport systems share a highly-polarized route of CSF influx along the periarterial space, an efflux path along the perivenous space, and a final fluid collection site by the dural and cervical lymphatic vessels. The two efflux pathways merge; tracers injected in either the eye or the brain are eventually trapped in cervical lymph nodes, and exchange or watershed zones between CSF and intraocular fluid in the retrobulbar optic nerve may explain some of the proclivities for disease to affect this region (19).

The similarities between the brain and ocular glymphatic systems also extend to the molecular mechanisms facilitating fluid transport. In the brain, AQP4 is highly polarized toward the vascular end feet of astrocytes, and orthogonal arrays of AQP4 constitute as much as 50% of the surface of their plasma membrane facing the vessel wall (35, 61).

Expectedly, AQP4 has been shown to facilitate both glymphatic CSF influx and clearance (3, 35, 36). In the eye, radial Müller cells spanning the neuroretina express similarly abundant AQP4 on perivascular end foot membranes, as well as in their processes facing the vitreous (62). Fibrous astrocytes along the optic nerve also express AQP4, and we show here that efflux of hAβ, similar to the brain, was facilitated by AQP4 in both the retina and the optic nerve. However, the ocular fluid transport system is distinctly different from the brain at lamina cribrosa. The hydraulic barrier provided by the lamina cribrosa permits higher pressure in the intraocular compartment than the intracranial one. The human lamina cribrosa is composed mainly of a meshwork of collagen and elastin fibers and penetrated by RGC axons and retinal vessels. In rodents, the lamina is composed primarily of astrocytes, whose processes wrap tightly around the RGC axons, forming a barrier that excludes the passage of even low molecular weight dextrans. Astrocytes in the lamina cribrosa are notably devoid of AQP4 and other aquaporins except for the metabolite permeable aquaglyceroporin AQP9 (62, 63). The unique lack of AQP4 in astrocytes of the lamina cribrosa may be a manifestation of the need to restrict fluid transfer between the perivascular space and the optic nerve at this junction, which is critical for maintaining a pressure difference (62). The lack of astrocytic AQP4 at the lamina could guide axonal fluid transport by restricting water permeability along alternative routes surrounding or within the astrocytes. Thus, although the brain and ocular glymphatic systems share key features, including polarization of fluid transport and a dependence on AQP4, it is clear the ocular glymphatic system is specialized around the lamina cribrosa barrier. We document that the lamina cribrosa effectively prevents efflux of extracellular tracers delivered to the vitreous compartment. Only tracers taken up by RGCs (hAβ, cadaverine, and K^+-analog $^{86}Rb^+$) and transported along their axons could pass the lamina barrier. Extracellular tracers, such as dextrans, were only able to enter the nerve in glaucomatous eyes with lamina defects (64). It cannot be excluded that the increased hAβ tracer signal in the optic nerve of 11-month-old DBA mice reflected a decreased influx of CSF in the optic nerve as reported by Mathieu et al. (22). However, the finding that glaucoma is associated with openings in the lamina cribrosa that allow passage of extracellular tracers does not support the idea that CSF washout plays a role in efflux of tracers intravitreally delivered to the optic nerve. As shown by the Yucel laboratory (22) and confirmed here, the lamina cribrosa also effectively inhibits periarterial influx of CSF tracers into the retina. In the brain, no such barrier has been described, and CSF tracers distribute brain-wide, albeit with regional differences in influx kinetics (3).

Our most unexpected observation is that accumulation of APP and Aβ in experimental glaucoma is not the consequence of reduced outflow. An unexpected, excessive tracer efflux along the optic nerve was observed in two distinct models of glaucoma. Such excessive flow, because of the destruction of the glial barrier at the lamina, leads to unspecific tracer efflux via the extracellular space, which we propose results in stagnation of the intra-axonal transport of APP and its cleavage product, Aβ. Considering the net decrease of outflow facility known to occur in glaucoma, the posterior efflux route described here makes a smaller contribution to the overall outflow than anterior routes (65). However, the functional importance of this smaller volume should not be underestimated, as it may be critical for fluid and waste elimination from the retina and optic nerve (19).

The discovery of an ocular glymphatic system as a fluid efflux path may shed new light on several pathologies in the eye. Up to 2.4% of the general population have a subclinical build-up of amyloid and other wastes in the ONH (ONH drusen), which is seen more frequently in patients with narrow scleral canals (66). Age-related macular degeneration, a major cause of visual loss, is also characterized by subretinal build-up of waste products, including amyloid in drusenoid deposits (67). Another major cause of blindness, glaucoma, was directly examined in this study. We speculate that abnormal transport of APP/Aβ or other metabolites driven by the increase in translaminar pressure contributes to the degeneration of RGC axons in early stages of glaucoma or after optic nerve injury (68, 69). In addition, the pathological increase in extracellular ocular fluid fluxes along the nerve in later-stage glaucoma might trigger additional stress in the form of both heightened metabolic demands and loss of essential cytosolic components, such as vitamin B_3 (70). Another important yet currently unresolved aspect of glaucoma is the large proportion (30-40%) of patients with demonstrable glaucomatous optic nerve damage who lack elevated IOP (71). We here propose the hypothesis that structural weakness or defects in the lamina cribrosa can lead to glaucoma in the absence of increased IOP, since the long-term redirection of glymphatic outflow from the intra-axonal to extracellular space may lead to the degeneration of RGCs (19, 64).

It is important to consider the limitations of this report. Our analysis demonstrates the existence of an ocular glymphatic clearance path in several strains of mice and rats. Because of the close anatomical and physiological resemblance to human ocular drainage (72, 73), rodent models have been extensively used in the study of glaucoma pathophysiology and have proven valuable for drug screening (43, 45, 46, 70, 74). Nevertheless, examination using a primate model of glaucoma would be important in future studies. Another potential caveat is that most of the data are collected postmortem after harvesting the eye and optic nerve. Microscopic resolution is needed to map the cellular details of the flow, yet it is not possible to image tracer transport along the distal optic nerve in vivo because the nerve is solidly embedded in the skull. We did, however, collect a set of in vivo observations supporting the model proposed in fig. S9. Using a funduscope, we imaged real-time dispersion of cadaverine after administration in the suprachoroidal space. The analysis showed that cadaverine was transported along the optic nerve similarly to the ex vivo observations. Alternative approaches, such as magnetic resonance or positron emission tomography, may allow for real-time in vivo imaging of ocular transport. However, such studies will require identification of contrast agents or positron emission tomography tracers taken up by RGCs. Alternatively, improvement of the resolution of proton (water) diffusion by magnetic resonance imaging (MRI) is of particular interest because the movement of fluid is key to understanding the ocular glymphatic system. Imaging of protons will also avoid the use of invasive vitreous injections. A limitation of this and other reports is the use of tracers to indirectly map fluid transport. The main observation reported is that tracers that exhibit cellular uptake (hAβ, cadaverine, and $^{86}Rb^{+}$) can pass the lamina cribrosa, which acts as a barrier for extracellular tracers, such as dextran and ovalbumin. We observed that hAβ transport was restricted to axons, consistent with the avid neuronal uptake of hAβ (29). However, it is possible that tracers taken up by astrocytes, such as cadaverine and $^{86}Rb^{+}$, also are transported across the lamina cribrosa via the astrocytic cytosol. We were concerned

that vitreous injections could artificially contribute to tracer transport, but we conclude based on the arguments listed below that our methodology did not in fact lead to artefactual tracer dispersion. We show that the distribution of hAβ is independent of (i) total volume injected and (ii) rate of infusion. Moreover, (iii) our infusion protocol does not increase IOP, and (iv) rats with much larger eyes exhibit the same pattern of hAβ transport as mice, including acceleration of transport in response to light stimulation. Last, the presence of intravitreal-injected tracers in the cervical lymph nodes does not prove that the tracers reached the cervical lymphatic system only by transport along the optic nerve. Efflux of ocular fluid from trabecular and uveoscleral pathways also accumulates in cervical lymph nodes (2, 34). The analysis of cervical lymph nodes was included here to outline the entire ocular export pathway.

Toxicity of Aβ was not a limitation of the study. An in-depth analysis of two eyes from the same mouse injected with either vehicle or hAβ tracer found no evidence of either reactive astrogliosis or microgliosis or caspase-3 activation. We also found no sign of BRB opening in response to vitreous administration of hAβ. A screen for 32 cytokines/chemokines showed that our protocol for hAβ intravitreal tracer injection did not evoke an immune response within the experimental time frame. Earlier reports have noted that subretinal injection and prolonged exposure to elevated amounts of hAβ (days to weeks) can induce toxicity (75, 76), but such effects were not noted in our study, which was limited to at most 2 hours exposure to hAβ. Thus, we are confident that the current study design likely avoided activation of hAβ-induced pathological processes. Together, our analysis provides the evidence for the existence of a highly-polarized ocular clearance system that might have implications for our understanding of eye health and disease.

Materials and Methods

Study design

The goal of this study was to understand how the metabolically active retina and optic nerve, being both devoid of lymphatics and distant from traditional ocular fluid efflux mechanisms, handle waste and fluid. By injecting multiple biologically-relevant or inert tracers into the vitreous, with which the retina directly and freely exchanges fluid, we anatomically characterized an eye-to-CSF clearance pathway that resembles the brain's glymphatic. We then sought to evaluate how physiological conditions of the ocular system interact with this clearance system by applying visual stimulation or manipulating the TPD. Finally, using two distinct murine models of glaucoma, we examined how waste/fluid handling changed in pathological conditions.

Animal sample sizes were calculated on the basis of a pilot study. Outlier detection based on the ROUT method (77) was performed before statistical analysis with confidence threshold, Q = 0.1%. Mice with initial IOP > 55 mmHg following CLS were excluded because this amplitude of IOP increase can impair retinal perfusion (46). Animals were randomly assigned and blinded to individuals carrying out analysis. Group and sample sizes for each experiment are indicated in the figure legends.

Experimental animals

Adult 2- to 12-month-old C57BL/6J, NG2-DsRed, Glt-1-Egfp(enhanced green fluorescent protein), FVB, DBA/2J , DBA/2J-*Gpnmb*$^{+}$/SjJ and CD-1 mice of either sex (the Jackson laboratory or Charles River Laboratories) and 2-month-old Brown Norway rats (Charles River Laboratories) were used. *Aqp4*$^{-/-}$ mice were generated as described (78). Prox-1-GFP mice were generated as described (79). C57BL/6J mice were used if not otherwise noted. All rodents were bred and housed in standard housing conditions at the Universities of Copenhagen, Rochester, or California, Berkeley in temperature-controlled rooms at 24°C with a normal 12-hour light/12-hour dark cycle. The animals had free access to food and water. Age-matched mice from both C57BL/6J and DBA/2J-*Gpnmb*$^{+}$/SjJ (D2-controls) strains were used as controls for the DBA/2J strain. We did not observe any differences between C57BL/6J and D2-control mice young or old age (table S2), indicating comparable glial lamina integrity between these two groups. The CLS model was adapted from Liu et al. (46, 80). Briefly, CD-1 mice were anesthetized as described below, and a suture was transconjunctivally passed around the equator of the eye with suture tension adjusted to achieve the desired IOP increase. Suture was kept for 1 month. Age-matched CD-1 mice without the surgical procedure were used as controls for the CLS model. All procedures were approved and in accordance with the guidelines of institutional Animal Care and Use Committee and the National Institutes of Health Guide for the Care and Use of Laboratory Animals at all universities. The experiments were designed to minimize the number of animals used.

In vivo intravitreal, suprachoroidal, and intracisternal tracer injection

All rodents were anesthetized with a ketamine and xylazine cocktail (100 mg/kg and 20 mg/kg, respectively). Once reflexes had ceased, rodents were mounted in a stereotactic head frame with body temperature maintained by a heating pad (Harvard Apparatus). A conjunctival peritomy was performed to expose the sclera at 11 o'clock to 1 o'clock. A 34-gauge needle connected to PE20 tubing and a Hamilton syringe was inserted into the vitreous chamber 1-2 mm posterior to the corneoscleral junction about 1-2 mm deep. In a subset of mice, a 30-gauge needle was inserted into the suprachoroidal space about 2 mm behind the limbus (81). To map lymphatic drainage 3 hours following intravitreal tracer injection of hAβ-647, mice were imaged with a fluorescence stereomicroscope (MVX10, Olympus) in the supine position. The cervical region was exposed before imaging. We pre-labeled mouse cervical lymph nodes by bilateral injection of fluorescein into the mouse cheek as described (33). One microliter [0.5% (w/v), diluted in phosphate-buffered saline (PBS)] (3, 82) of one of the following tracers was injected intravitreally, suprachoroidally or intracisternally (table S3) over a period of either 5 or 10 min by a syringe pump (11 Plus, Harvard Apparatus): HiLyte Fluor 488-, HiLyte Fluor 555-, or HiLyte Fluor 647-conjugated hAβ (1-40, AnaSpec), FITC-conjugated cadaverine (Thermo Fisher Scientific) (83, 84), FITC-, Texas Red-, Alexa Fluor (AF) 488- or AF 555-conjugated dextrans (3 kDa, 10 kDa, 500 kDa, referred to as AF-dextran for simplicity) (Thermo Fisher Scientific), or FITC-ovalbumin (Thermo Fisher Scientific) (Fig. 1A). In a subset of mice, 0.3 μl of1.67% (w/v) HiLyte Fluor 488-conjugated hAβ (1-40, AnaSpec) was injected to control for the effect of injection volume. We saw no statistical differences in hAβ tracer distribution between the 5 and 10 min injections with respect to fluorescent signal and peak intensity (n = 6-8, P =

0.527-0.649, unpaired two-tailed *t*-test). A needle holder attached to a hand manipulator (World Precision Instrument) was used to secure the needle in position for the duration of the experiment. An eye lubricant (GenTeal Lubricant Eye Gel, Alcon) was applied to the cornea during the experiment. Photopic flicker (1 Hz, 100 ms and five lumens) from a light-emitting diode (LED) light source (Pelican L4) was used to stimulate the tracer-injected eye under control of a Master 8 stimulator (A.M.P.I.). We monitored both the lens and retina in all injection experiments and did not observe damage in any animals. A subset of 1 Hz light-stimulated mice was treated with 1% atropine (Sigma-Aldrich) by topical instillation to the stimulated eye. A subset of dark, unstimulated mice was treated with 2% pilocarpine (Sigma-Aldrich) by topical instillation. During the experiment, the pupil sizes of subsets of mice from the dark, unstimulated, 1 Hz light-stimulated, and atropine-treated groups were tracked by an infrared camera (DCC3240N, Thorlabs). Intracisternal injections were performed in anesthetized mice fixed in a stereotactic frame. A 30-gauge needle was inserted into the CM, and 0.5% AF-dextran (Thermo Fisher Scientific) was infused at a rate of 1.5 μl/min over 10 min with a syringe pump (Harvard Apparatus).

Ultimate 3D imaging of solvent-cleared organs (uDISCO)

One hour after intravitreal injection of hAβ-HiLyte-647, anesthetized mice were transcardially perfused with heparinized PBS followed by 4% formaldehyde. After 24 hours post-fixation in 4% formaldehyde, uDISCO was performed as previously described (26). Subsequently, the transparent mouse heads were imaged at a z-interval of 10 μm using a LaVision BioTec Ultramicroscope II light-sheet microscope with an Olympus MV PLAPO 1x air-objective and MVX10 0.63x zoom body. Amira software 6.3.0 was used for tracing and 3D-reconstruction of the hAβ signal in eye and optic nerve.

Intravascular tracer administration and quantification

10 μl of isotonic saline containing the K^+-analog $^{86}Rb^+$ (0.1 μCi/μl, PerkinElmer) was injected into the right internal carotid artery along with ^3H-mannitol (0.1 μCi/μl, American Radiolabeled Chemicals) over two sec through a catheter connected to a syringe pump (Harvard Apparatus). The ipsilateral eye and optic nerve were quickly dissected, and the nerve was separated into proximal and distal parts of equal length. Radioactivity was measured using a multipurpose scintillation counter (Beckman Coulter) after overnight solubilization at 45°C in Soluene (PerkinElmer) and scintillation counting with Hionic Fluor cocktail (PerkinElmer). $^{86}Rb^+$ counts were plotted after subtraction of counts in the contralateral eye and optic nerve. FITC-cadaverine (100 μl, 0.5%, Thermo Fisher Scientific) was administered to anesthetized C57BL/6J mice through a catheter inserted through the external carotid artery into the right internal carotid artery exposed as described earlier (85), and tissue was harvested 10 min later. Fresh eye and nerve were immediately imaged with a naïve control (C57BL/6J without injection) under a fluorescence stereomicroscope (MVX10, Olympus) using a digital camera (C11440, Hamamatsu) controlled by MetaMorph software (Molecular Devices). Retina flat-mounts were prepared as described before (86), and images were collected using a confocal microscope after fixation with Bouin solution.

Imaging and quantification of tracer transport

For macroscopic imaging of tracer transport, the freshly harvested nerves obtained from anesthetized mice after removal of brain tissue were imaged using the stereofluorescent microscope described above. A pE LED (PRIOR Lumen 1600-LED) fluorescent light intensity of 95% and exposure time of 1000 ms were kept constant across all groups. Fluorescent intensity was quantified with arbitrary units (A.U.). After intravitreal injection, the ipsilateral and contralateral nerves were imaged simultaneously. After subtracting the mean fluorescent intensity of the control nerve, the fluorescent intensity profile of the tracer-exposed mouse or rat optic nerve was quantified at 3.09 μm or 6.76 μm steps, respectively, using a custom-made MATLAB (MathWorks) script. CD-1 mouse optic nerves were imaged with an Axio Imager M1 epifluorescence deconvolution microscope (Carl Zeiss AG) and quantified at 2.13 μm steps. Fluorescence as a function of distance from the eye was then used for further quantifications. Total fluorescence of tracer transport was obtained by calculating the trapezoidal numerical integration of the function. Peak intensity was the highest value of the fluorescent intensity profile. Movement distance was defined as the length of the wavefront of signal in the experimental nerve that exceeded the mean intensity of the control nerves by three standard deviations. A confocal scanning microscope attached to an inverted microscope (IX81, Olympus) controlled by Olympus Fluoview 500 software was used to map the cellular and subcellular hAβ tracer distribution using the whole-mount preparations or 20 μm cryosections. For mice that received suprachoroidal injections, *in vivo* retinal imaging was recorded by a fundus camera (Micro III, Phoenix Research Laboratories).

Fluorescence immunocytochemistry

Mice were anesthetized and transcardially perfused with 4% formaldehyde (Sigma-Aldrich). Wheat germ agglutinin (lectin) tagged with AF-647 (Fisher Scientific W32466) was diluted in PBS to a final concentration of 12.5 μg/ml to label the blood vessel lumen in select experiments. Dural whole-mout, retina whole mount or mouse optic nerve was carefully dissected and was post-fixed in 4% formaldehyde for 2 hours at room temperature. Serial 20 μm tissue sections were obtained using a cryostat (Leica CM190) after sucrose gradients ending with 30% sucrose. Sections were incubated overnight at 4°C with a single or combination of the following primary antibodies: rabbit anti-mouse LYVE-1, (1:200, Abcam, ab14917-100), rat anti-LYVE1 (ALY7) (1:250, eBioscience 14-0443-83), rabbit anti-RNA-binding protein with multiple splicing (RBPMS) (1:250, GeneTex 118619) (87), mouse anti-TUJ1 (1:500, Covance MMS-435P), rabbit anti-APP (1:500, Abcam ab15272), Syrian hamster anti-podoplanin (PDPN) (1:100 eBioscience, clone 8.1.1), rabbit anti-AQP4 (1:500, Millipore AB3594), goat anti-VEGFR3 (1:500, R&D Systems AF743), goat anti-OLIG2 (1:500, R&D Systems AF2418), mouse anti-glutamine synthetase (GS) (1:500, Chemicon International Inc, MAB302), mouse anti-AP-2α (1:500, DSHB Hybridoma Product 3B5 [deposited by Williams, T.J.]), rat anti-mouse CD68 (1:500, BioRad MCA1957, hydrocephalus brain slice was used as positive control), mouse anti-glial fibrillary acidic protein (GFAP) (1:500, Millipore MAB360), rabbit anti-caspase-3 (8G10) (1:500, Cell Signaling Technology 9665S, P1 mouse pup brain with ongoing pruning was used as positive control), and goat anti-hOtx2 (1:40, R&D Systems AF1979). The primary antibodies were detected with appropriate AF-488-, 594-, 647-conjugated or Cy2-, Cy3-,

Cy5-conjugated secondary antibodies (1:500, Molecular Probes/Jackson ImmunoResearch) after 2 hours of incubation at room temperature. ProLong Gold containing 4′,6-diamidino-2-phenylindole (DAPI) (Invitrogen, P16931) was used for mounting the sections.

IOP and ICP measurement and manipulation

IOP of the rodent's eye was measured by a rebound tonometer (Icare, TONOLAB). Briefly, anesthetized rodents were placed in a prone position. Five to ten measurements at 5 min after anesthesia induction were taken for each rodent to get the baseline. In a subset of mice, we also continuously monitored IOP in an experimental group and compared to a sham surgery group in which only the fluid infusion was withheld. In another subset, mouse IOP was measured while their ICP was manipulated from baseline (see below) and normalized to the IOP value without ICP manipulation. In another group, IOP was monitored by intracameral tonometry (88) via cannulation to the anterior chamber with a 36-gauge needle. ICP was monitored through a CM catheter sealed to the skull with dental cement (Stoelting Co). Intracameral IOP and ICP were monitored by a pressure transducer (WPI) connected to a pressure monitor (WPI), acquired at 10,000 Hz, digitized, and recorded continuously for the duration of the experiment with a DigiData 1332A and PClampex9.2 software (Axon Instruments) and then downsampled to 100 Hz. To calculate the power of 1 Hz in IOP, signal between 0.99 Hz and 1.01 Hz was used. To elevate the mouse's ICP, we infused 538 ± 76.8μl aCSF over 30min into the CM through a Hamilton syringe connected to a syringe pump (Harvard Apparatus). ACSF contained the following (in mM): 155 NaCl, 3.5 KCl, 1 $CaCl_2$, 1 $MgCl_2$, and 2 NaH_2PO_4, pH 7.4, 300 mOsm. To lower ICP, we actively withdrew 37 ± 5.1μl CSF over 30min via a surgical opening in the CM. ICP was monitored in real-time during ICP manipulation. Intravitreal tracer injection was initiated 5 min after ICP stabilized.

Electron microscopy

D2-control and DBA/2J mice were fixed by transcardial perfusion with 0.5% glutaraldehyde and 4% formaldehyde in 0.1 M phosphate buffer (pH 7.4, 9 ml/min for 25 min). The eye and optic nerve were post-fixed for 2 hours with 4% formaldehyde, and 1% glutaraldehyde in 0.1 M PBS before 50 μm coronal sections were dissected and embedded in Durcupan (Sigma-Aldrich). A PowerTome XL (RMC Boeckeler) was used to prepare ultrathin sections, and a transmission electron microscope (Hitachi H-7650) attached to a charge-coupled device camera (Gatan Inc. ES1000W) was used to examine the glial lamina region of the ONH at a nominal magnification of 4200x.

Real-time tetramethylammonium (TMA^+) iontophoresis

Optic nerves from anesthetized mice were quickly dissected after decapitation and immersed for 60 min in oxygenated aCSF at room temperature. Microelectrodes were fabricated from double-barreled theta-glass using a tetraphenylborate-based ion exchanger. The TMA^+ barrel was backfilled with 150 mM TMA-chloride, while the reference barrel contained 150 mM NaCl and 10 μM AF-594. A series of currents of 20 nA, 40 nA, 80 nA, and 100 nA was applied by a dual-channel microelectrode preamplifier. The electrode tips were kept ~150 μm apart. The TMA^+ signal was calculated by subtracting the voltage measured by the reference barrel from the voltage measured by the ion-detecting barrel. Nikolsky equation

was used for calibration of the TMA^+ electrodes based on measurements obtained in electrodes containing standards of 0.5, 1, 2, 4, and 8 mM TMA-chloride in 150 mM NaCl. The TMA^+ measurements were acquired relative to similar recordings obtained in 0.3% agarose prepared from a solution containing 0.5 mM TMA^+ and 150 mM NaCl. "Walter" (developed by C. Nicholson) was used to calculate α (volume fraction: ratio of extracellular space volume to total tissue volume) and λ (tortuosity: square root of the ratio of free diffusion coefficient to apparent diffusion coefficient) using the Nikolsky equation (89).

Cytokine assay

Thirty minutes after intravitreal injection of hAβ or vehicle in opposite eyes of the same animal, mice were transcardially perfused with ice-cold PBS. Retinas were dissected and homogenized in extraction buffer (20 mM Tris pH 7.4, 150 mM NaCl, and 0.5% Tween-20 in PBS) with a 1:100 dilution of protease inhibitor cocktail (Sigma-Aldrich P8340). The soluble fraction after centrifugation was analyzed by Eve Technologies (Alberta, Canada) using the Multiplex Laser Bead platform.

BRB permeability assay

Thirty or 120 minutes after intravitreal injection of hAβ or vehicle in opposite eyes of the same animal, mice were intravenously infused with Evans blue (2%, 2 ml/kg) before fixation and confocal imaging. In a subset of mice, Evans blue leakage from the blood into the retina was measured as described before (90).

Statistical analysis

Statistical analysis was performed with the aid of GraphPad Prism 6.0c (GraphPad Software). The normality of the data was tested by Kolmogorov Smirnov test. For variables that passed the normality test (at significance level of α=0.05), parametric statistical methods, such as the two-sample Welch *t*-test (for comparing the mean equality of two samples) or one-way ANOVA *F*-test (for testing mean equality among more than two groups), were employed. Following one-way analysis of variance (ANOVA) analyses, Tukey's or Dunnett's *post hoc* analyses were performed to identify significant pairwise group mean differences. For those variables that did not pass the normality test, nonparametric methods, such as the Mann-Whitney *U* test (for independent two-group comparisons), Wilcoxon signed-rank test (for comparing matched samples), or Kruskal-Wallis test (for comparing multiple groups), were used instead. Following Kruskal-Wallis one-way ANOVA, Dunn's *post hoc* analyses were performed to detect significant pairwise group median differences. Two-way ANOVA followed by Sidak's multiple comparisons was performed when two different categorical independent variables were assessed. A significance level of α=0.05 was used in all statistical tests performed in this study. Values are expressed as the mean ± SEM if not otherwise stated.

Supplementary Material

Refer to Web version on PubMed Central for supplementary material.

Acknowledgements:

We thank Karen L. Bentley and Gayle Schneider from the URMC Electron Microscope Research Core Facility, Wei Song, Shinya Sakurai and Jinwook Jung for technical support; Charles Nicholson for discussions, Vinita Rangroo Thrane and Paul Cumming for comments on the manuscript, and Dan Xue for graphic illustrations and animations. We thank Xing Qiu and Jiatong Sui for their statistical expertise. We thank Young K. Hong at University of Southern California and the Mutant Mouse Regional Resource Centers (MMRRC) for providing the founder mice of prox1-GFP.

Funding: This project has received funding from the European Research Council (ERC) under the European Union's Horizon 2020 research and innovation programme (grant agreement no. 742112), the Novo Nordisk and the Lundbeck Foundations, Dr. Miriam and Sheldon G. Adelson Medical Research Foundation, the NIH/NINDS/NIA/NEI (R01NS100366, RF1AG057575, R01EY028995), the Research to Prevent Blindness Foundation (Dr. Nedergaard is a recipient of a Research to Prevent Blindness Stein Innovation Award) and the Cure Alzheimer's Fund. Western Norway Regional Health Authority (Helse Vest grants nos. 912179 and 912230), Norwegian Glaucoma Research Foundation. The content is solely the responsibility of the authors and does not necessarily represent the official views of the sponsors.

References and Notes

1. Aukland K, Reed RK, Interstitial-lymphatic mechanisms in the control of extracellular fluid volume. Physiological reviews 73, 1–78 (1993). [PubMed: 8419962]
2. Yucel YH, Johnston MG, Ly T, Patel M, Drake B, Gumus E, Fraenkl SA, Moore S, Tobbia D, Armstrong D, Horvath E, Gupta N, Identification of lymphatics in the ciliary body of the human eye: a novel "uveolymphatic" outflow pathway. Experimental eye research 89, 810–819 (2009). [PubMed: 19729007]
3. Iliff JJ, Wang M, Liao Y, Plogg BA, Peng W, Gundersen GA, Benveniste H, Vates GE, Deane R, Goldman SA, Nagelhus EA, Nedergaard M, A paravascular pathway facilitates CSF flow through the brain parenchyma and the clearance of interstitial solutes, including amyloid beta. Science translational medicine 4, 147ra111 (2012).
4. Louveau A, Smirnov I, Keyes TJ, Eccles JD, Rouhani SJ, Peske JD, Derecki NC, Castle D, Mandell JW, Lee KS, Harris TH, Kipnis J, Structural and functional features of central nervous system lymphatic vessels. Nature 523, 337–341 (2015). [PubMed: 26030524]
5. Aspelund A, Antila S, Proulx ST, Karlsen TV, Karaman S, Detmar M, Wiig H, Alitalo K, A dural lymphatic vascular system that drains brain interstitial fluid and macromolecules. The Journal of experimental medicine 212, 991–999 (2015). [PubMed: 26077718]
6. Ahn JH, Cho H, Kim JH, Kim SH, Ham JS, Park I, Suh SH, Hong SP, Song JH, Hong YK, Jeong Y, Park SH, Koh GY, Meningeal lymphatic vessels at the skull base drain cerebrospinal fluid. Nature 572, 62–66 (2019). [PubMed: 31341278]
7. Eide PK, Vatnehol SAS, Emblem KE, Ringstad G, Magnetic resonance imaging provides evidence of glymphatic drainage from human brain to cervical lymph nodes. Scientific reports 8, 7194 (2018). [PubMed: 29740121]
8. Absinta M, Ha SK, Nair G, Sati P, Luciano NJ, Palisoc M, Louveau A, Zaghloul KA, Pittaluga S, Kipnis J, Reich DS, Human and nonhuman primate meninges harbor lymphatic vessels that can be visualized noninvasively by MRI. eLife 6, (2017).
9. Myllyla T, Harju M, Korhonen V, Bykov A, Kiviniemi V, Meglinski I, Assessment of the dynamics of human glymphatic system by near-infrared spectroscopy. Journal of biophotonics 11, e201700123 (2018). [PubMed: 28802090]
10. Ringstad G, Vatnehol SAS, Eide PK, Glymphatic MRI in idiopathic normal pressure hydrocephalus. Brain : a journal of neurology 140, 2691–2705 (2017). [PubMed: 28969373]
11. Kiviniemi V, Wang X, Korhonen V, Keinanen T, Tuovinen T, Autio J, LeVan P, Keilholz S, Zang YF, Hennig J, Nedergaard M, Ultra-fast magnetic resonance encephalography of physiological brain activity - Glymphatic pulsation mechanisms? Journal of cerebral blood flow and metabolism : official journal of the International Society of Cerebral Blood Flow and Metabolism 36, 1033–1045 (2016).
12. Nedergaard M, Neuroscience. Garbage truck of the brain. Science (New York, N.Y.) 340, 1529–1530 (2013).

13. Koronyo Y, Biggs D, Barron E, Boyer DS, Pearlman JA, Au WJ, Kile SJ, Blanco A, Fuchs DT, Ashfaq A, Frautschy S, Cole GM, Miller CA, Hinton DR, Verdooner SR, Black KL, Koronyo-Hamaoui M, Retinal amyloid pathology and proof-of-concept imaging trial in Alzheimer's disease. JCI insight 2, (2017).
14. Kang JE, Lim MM, Bateman RJ, Lee JJ, Smyth LP, Cirrito JR, Fujiki N, Nishino S, Holtzman DM, Amyloid-beta dynamics are regulated by orexin and the sleep-wake cycle. Science (New York, N.Y.) 326, 1005–1007 (2009).
15. Holth JK, Fritschi SK, Wang C, Pedersen NP, Cirrito JR, Mahan TE, Finn MB, Manis M, Geerling JC, Fuller PM, Lucey BP, Holtzman DM, The sleep-wake cycle regulates brain interstitial fluid tau in mice and CSF tau in humans. Science (New York, N.Y.) 363, 880–884 (2019).
16. Yamamoto K, Tanei ZI, Hashimoto T, Wakabayashi T, Okuno H, Naka Y, Yizhar O, Fenno LE, Fukayama M, Bito H, Cirrito JR, Holtzman DM, Deisseroth K, Iwatsubo T, Chronic optogenetic activation augments abeta pathology in a mouse model of Alzheimer disease. Cell Rep 11, 859–865 (2015). [PubMed: 25937280]
17. Xie L, Kang H, Xu Q, Chen MJ, Liao Y, Thiyagarajan M, O'Donnell J, Christensen DJ, Nicholson C, Iliff JJ, Takano T, Deane R, Nedergaard M, Sleep drives metabolite clearance from the adult brain. Science (New York, N.Y.) 342, 373–377 (2013).
18. Denniston AK, Keane PA, Paravascular Pathways in the Eye: Is There an 'Ocular Glymphatic System'? Invest Ophthalmol Vis Sci 56, 3955–3956 (2015). [PubMed: 26087361]
19. Wostyn P, De Groot V, Van Dam D, Audenaert K, Killer HE, De Deyn PP, The Glymphatic Hypothesis of Glaucoma: A Unifying Concept Incorporating Vascular, Biomechanical, and Biochemical Aspects of the Disease. BioMed research international 2017, 5123148 (2017). [PubMed: 28948167]
20. Petzold A, Retinal glymphatic system: an explanation for transient retinal layer volume changes? Brain : a journal of neurology 139, 2816–2819 (2016). [PubMed: 29106485]
21. Wostyn P, Van Dam D, Audenaert K, Killer HE, De Deyn PP, De Groot V, A new glaucoma hypothesis: a role of glymphatic system dysfunction. Fluids Barriers CNS 12, 16 (2015). [PubMed: 26118970]
22. Mathieu E, Gupta N, Ahari A, Zhou X, Hanna J, Yucel YH, Evidence for Cerebrospinal Fluid Entry Into the Optic Nerve via a Glymphatic Pathway. Invest Ophthalmol Vis Sci 58, 4784–4791 (2017). [PubMed: 28973323]
23. Mathieu E, Gupta N, Paczka-Giorgi LA, Zhou X, Ahari A, Lani R, Hanna J, Yucel YH, Reduced Cerebrospinal Fluid Inflow to the Optic Nerve in Glaucoma. Invest Ophthalmol Vis Sci 59, 5876–5884 (2018). [PubMed: 30543343]
24. Ito Y, Shimazawa M, Tsuruma K, Mayama C, Ishii K, Onoe H, Aihara M, Araie M, Hara H, Induction of amyloid-beta(1–42) in the retina and optic nerve head of chronic ocular hypertensive monkeys. Molecular vision 18, 2647–2657 (2012). [PubMed: 23170058]
25. Loffler KU, Edward DP, Tso MO, Immunoreactivity against tau, amyloid precursor protein, and beta-amyloid in the human retina. Invest Ophthalmol Vis Sci 36, 24–31 (1995). [PubMed: 7822152]
26. Pan C, Cai R, Quacquarelli FP, Ghasemigharagoz A, Lourbopoulos A, Matryba P, Plesnila N, Dichgans M, Hellal F, Erturk A, Shrinkage-mediated imaging of entire organs and organisms using uDISCO. Nature methods 13, 859–867 (2016). [PubMed: 27548807]
27. Armulik A, Genove G, Mae M, Nisancioglu MH, Wallgard E, Niaudet C, He L, Norlin J, Lindblom P, Strittmatter K, Johansson BR, Betsholtz C, Pericytes regulate the blood-brain barrier. Nature 468, 557–561 (2010). [PubMed: 20944627]
28. Murfee WL, Skalak TC, Peirce SM, Differential arterial/venous expression of NG2 proteoglycan in perivascular cells along microvessels: Identifying a venule-specific phenotype. Microcirculation 12, 151–160 (2005). [PubMed: 15824037]
29. Kanekiyo T, Cirrito JR, Liu CC, Shinohara M, Li J, Schuler DR, Shinohara M, Holtzman DM, Bu G, Neuronal clearance of amyloid-beta by endocytic receptor LRP1. J Neurosci 33, 19276–19283 (2013). [PubMed: 24305823]
30. Gausas RE, Gonnering RS, Lemke BN, Dortzbach RK, Sherman DD, Identification of human orbital lymphatics. Ophthalmic Plast Reconstr Surg 15, 252–259 (1999). [PubMed: 10432521]

31. Killer HE, Laeng HR, Groscurth P, Lymphatic capillaries in the meninges of the human optic nerve. J Neuroophthalmol 19, 222–228 (1999). [PubMed: 10608671]
32. Chen L, Ocular lymphatics: state-of-the-art review. Lymphology 42, 66–76 (2009). [PubMed: 19725271]
33. Mathieu E, Gupta N, Macdonald RL, Ai J, Yucel YH, In vivo imaging of lymphatic drainage of cerebrospinal fluid in mouse. Fluids Barriers CNS 10, 35 (2013). [PubMed: 24360130]
34. Yucel YH, Cardinell K, Khattak S, Zhou X, Lapinski M, Cheng F, Gupta N, Active Lymphatic Drainage From the Eye Measured by Noninvasive Photoacoustic Imaging of Near-Infrared Nanoparticles. Invest Ophthalmol Vis Sci 59, 2699–2707 (2018). [PubMed: 29860456]
35. Mathiisen TM, Lehre KP, Danbolt NC, Ottersen OP, The perivascular astroglial sheath provides a complete covering of the brain microvessels: an electron microscopic 3D reconstruction. Glia 58, 1094–1103 (2010). [PubMed: 20468051]
36. Mestre H, Hablitz LM, Xavier AL, Feng W, Zou W, Pu T, Monai H, Murlidharan G, Castellanos Rivera RM, Simon MJ, Pike MM, Pla V, Du T, Kress BT, Wang X, Plog BA, Thrane AS, Lundgaard I, Abe Y, Yasui M, Thomas JH, Xiao M, Hirase H, Asokan A, Iliff JJ, Nedergaard M, Aquaporin-4-dependent glymphatic solute transport in the rodent brain. eLife 7, (2018).
37. Morgan JE, Circulation and axonal transport in the optic nerve. Eye 18, 1089–1095 (2004). [PubMed: 15534594]
38. Nusbaum DM, Wu SM, Frankfort BJ, Elevated intracranial pressure causes optic nerve and retinal ganglion cell degeneration in mice. Experimental eye research 136, 38–44 (2015). [PubMed: 25912998]
39. Read SA, Collins MJ, Becker H, Cutting J, Ross D, Savill AK, Trevor B, Changes in intraocular pressure and ocular pulse amplitude with accommodation. The British journal of ophthalmology 94, 332–335 (2010). [PubMed: 19822912]
40. Jenssen F, Krohn J, Effects of static accommodation versus repeated accommodation on intraocular pressure. Journal of glaucoma 21, 45–48 (2012). [PubMed: 21173703]
41. Coleman DJ, On the hydraulic suspension theory of accommodation. Trans Am Ophthalmol Soc 84, 846–868 (1986). [PubMed: 3590482]
42. Weinreb RN, Aung T, Medeiros FA, The pathophysiology and treatment of glaucoma: a review. Jama 311, 1901–1911 (2014). [PubMed: 24825645]
43. Anderson MG, Smith RS, Hawes NL, Zabaleta A, Chang B, Wiggs JL, John SW, Mutations in genes encoding melanosomal proteins cause pigmentary glaucoma in DBA/2J mice. Nature genetics 30, 81–85 (2002). [PubMed: 11743578]
44. Libby RT, Anderson MG, Pang IH, Robinson ZH, Savinova OV, Cosma IM, Snow A, Wilson LA, Smith RS, Clark AF, John SW, Inherited glaucoma in DBA/2J mice: pertinent disease features for studying the neurodegeneration. Vis Neurosci 22, 637–648 (2005). [PubMed: 16332275]
45. Fernandes KA, Harder JM, Williams PA, Rausch RL, Kiernan AE, Nair KS, Anderson MG, John SW, Howell GR, Libby RT, Using genetic mouse models to gain insight into glaucoma: Past results and future possibilities. Experimental eye research 141, 42–56 (2015). [PubMed: 26116903]
46. Liu HH, Zhang L, Shi M, Chen L, Flanagan JG, Comparison of laser and circumlimbal suture induced elevation of intraocular pressure in albino CD-1 mice. PloS one 12, e0189094 (2017). [PubMed: 29190824]
47. Roberts MD, Grau V, Grimm J, Reynaud J, Bellezza AJ, Burgoyne CF, Downs JC, Remodeling of the connective tissue microarchitecture of the lamina cribrosa in early experimental glaucoma. Invest Ophthalmol Vis Sci 50, 681–690 (2009). [PubMed: 18806292]
48. Tehrani S, Johnson EC, Cepurna WO, Morrison JC, Astrocyte processes label for filamentous actin and reorient early within the optic nerve head in a rat glaucoma model. Invest Ophthalmol Vis Sci 55, 6945–6952 (2014). [PubMed: 25257054]
49. Ju WK, Kim KY, Lindsey JD, Angert M, Duong-Polk KX, Scott RT, Kim JJ, Kukhmazov I, Ellisman MH, Perkins GA, Weinreb RN, Intraocular pressure elevation induces mitochondrial fission and triggers OPA1 release in glaucomatous optic nerve. Invest Ophthalmol Vis Sci 49, 4903–4911 (2008). [PubMed: 18469184]

50. Wang R, Seifert P, Jakobs TC, Astrocytes in the Optic Nerve Head of Glaucomatous Mice Display a Characteristic Reactive Phenotype. Invest Ophthalmol Vis Sci 58, 924–932 (2017). [PubMed: 28170536]
51. Sykova E, Extrasynaptic volume transmission and diffusion parameters of the extracellular space. Neuroscience 129, 861–876 (2004). [PubMed: 15561404]
52. Goel M, Picciani RG, Lee RK, Bhattacharya SK, Aqueous humor dynamics: a review. Open Ophthalmol J 4, 52–59 (2010). [PubMed: 21293732]
53. Wostyn P, Van Dam D, De Deyn PP, Intracranial pressure and glaucoma: Is there a new therapeutic perspective on the horizon? Med Hypotheses 118, 98–102 (2018). [PubMed: 30037625]
54. Palkama AK, Velasquez D, Reynaud J, Thompson HW, Beuerman RW, Regulatory effect of pilocarpine and/or atropine on the facility of outflow in perfused bovine anterior eye segments and intact trabecular meshwork and ciliary. Invest Ophth Vis Sci 43, U900–U900 (2002).
55. Croft MA, Lutjen-Drecoll E, Kaufman PL, Age-related posterior ciliary muscle restriction - A link between trabecular meshwork and optic nerve head pathophysiology. Experimental eye research 158, 187–189 (2017). [PubMed: 27453343]
56. Christen R, Pache M, Teuchner B, Meyer P, Prunte C, Flammer J, Iris transillumination defects in patients with primary open angle glaucoma. European journal of ophthalmology 13, 365–369 (2003). [PubMed: 12872793]
57. Wostyn P, De Groot V, Van Dam D, Audenaert K, De Deyn PP, Killer HE, The Glymphatic System: A New Player in Ocular Diseases? Invest Ophthalmol Vis Sci 57, 5426–5427 (2016). [PubMed: 27768786]
58. Wostyn P, Killer HE, De Deyn PP, Glymphatic stasis at the site of the lamina cribrosa as a potential mechanism underlying open-angle glaucoma. Clinical & experimental ophthalmology 45, 539–547 (2017). [PubMed: 28129671]
59. Wostyn P, De Deyn PP, The “Ocular Glymphatic System”: An Important Missing Piece in the Puzzle of Optic Disc Edema in Astronauts? Invest Ophthalmol Vis Sci 59, 2090–2091 (2018). [PubMed: 29677371]
60. Wostyn P, De Winne F, Stern C, De Deyn PP, Dilated Prelaminar Paravascular Spaces as a Possible Mechanism for Optic Disc Edema in Astronauts. Aerosp Med Hum Perform 89, 1089–1091 (2018). [PubMed: 30487031]
61. Rash JE, Yasumura T, Direct immunogold labeling of connexins and aquaporin-4 in freeze-fracture replicas of liver, brain, and spinal cord: factors limiting quantitative analysis. Cell Tissue Res 296, 307–321 (1999). [PubMed: 10382274]
62. Nagelhus EA, Veruki ML, Torp R, Haug FM, Laake JH, Nielsen S, Agre P, Ottersen OP, Aquaporin-4 water channel protein in the rat retina and optic nerve: polarized expression in Muller cells and fibrous astrocytes. J Neurosci 18, 2506–2519 (1998). [PubMed: 9502811]
63. Naka M, Kanamori A, Negi A, Nakamura M, Reduced expression of aquaporin-9 in rat optic nerve head and retina following elevated intraocular pressure. Invest Ophthalmol Vis Sci 51, 4618–4626 (2010). [PubMed: 20357197]
64. Burgoyne CF, Downs JC, Bellezza AJ, Suh JK, Hart RT, The optic nerve head as a biomechanical structure: a new paradigm for understanding the role of IOP-related stress and strain in the pathophysiology of glaucomatous optic nerve head damage. Prog Retin Eye Res 24, 39–73 (2005). [PubMed: 15555526]
65. Sacca SC, Gandolfi S, Bagnis A, Manni G, Damonte G, Traverso CE, Izzotti A, The Outflow Pathway: A Tissue With Morphological and Functional Unity. J Cell Physiol 231, 1876–1893 (2016). [PubMed: 26754581]
66. Malmqvist L, Li XQ, Eckmann CL, Skovgaard AM, Olsen EM, Larsen M, Munch IC, Hamann S, Optic Disc Drusen in Children: The Copenhagen Child Cohort 2000 Eye Study. J Neuroophthalmol 38, 140–146 (2018). [PubMed: 28841585]
67. Anderson DH, Talaga KC, Rivest AJ, Barron E, Hageman GS, Johnson LV, Characterization of beta amyloid assemblies in drusen: the deposits associated with aging and age-related macular degeneration. Experimental eye research 78, 243–256 (2004). [PubMed: 14729357]

68. Buckingham BP, Inman DM, Lambert W, Oglesby E, Calkins DJ, Steele MR, Vetter ML, Marsh-Armstrong N, Horner PJ, Progressive ganglion cell degeneration precedes neuronal loss in a mouse model of glaucoma. J Neurosci 28, 2735–2744 (2008). [PubMed: 18337403]
69. Liu C, Zhang CW, Zhou Y, Wong WQ, Lee LC, Ong WY, Yoon SO, Hong W, Fu XY, Soong TW, Koo EH, Stanton LW, Lim KL, Xiao ZC, Dawe GS, APP upregulation contributes to retinal ganglion cell degeneration via JNK3. Cell death and differentiation 25, 661–676 (2018).
70. Williams PA, Harder JM, Foxworth NE, Cochran KE, Philip VM, Porciatti V, Smithies O, John SW, Vitamin B3 modulates mitochondrial vulnerability and prevents glaucoma in aged mice. Science (New York, N.Y.) 355, 756–760 (2017).
71. Sommer A, Tielsch JM, Katz J, Quigley HA, Gottsch JD, Javitt J, Singh K, Relationship between Intraocular-Pressure and Primary Open Angle Glaucoma among White and Black-Americans - the Baltimore Eye Survey. Arch Ophthalmol-Chic 109, 1090–1095 (1991).
72. Smith RS, Zabaleta A, Savinova OV, John SW, The mouse anterior chamber angle and trabecular meshwork develop without cell death. BMC developmental biology 1, 3–3 (2001). [PubMed: 11228591]
73. Johnson M, McLaren JW, Overby DR, Unconventional aqueous humor outflow: A review. Experimental eye research 158, 94–111 (2017). [PubMed: 26850315]
74. Dismuke WM, Overby DR, Civan MM, Stamer WD, The Value of Mouse Models for Glaucoma Drug Discovery. J Ocul Pharmacol Ther 32, 486–487 (2016). [PubMed: 26982549]
75. Dinet V, Bruban J, Chalour N, Maoui A, An N, Jonet L, Buret A, Behar-Cohen F, Klein C, Treton J, Mascarelli F, Distinct effects of inflammation on gliosis, osmohomeostasis, and vascular integrity during amyloid beta-induced retinal degeneration. Aging Cell 11, 683–693 (2012). [PubMed: 22577879]
76. Mohd Lazaldin MA, Iezhitsa I, Agarwal R, Bakar NS, Agarwal P, Mohd Ismail N, Time- and dose-related effects of amyloid beta1–40 on retina and optic nerve morphology in rats. Int J Neurosci 128, 952–965 (2018). [PubMed: 29488424]
77. Motulsky HJ, Brown RE, Detecting outliers when fitting data with nonlinear regression - a new method based on robust nonlinear regression and the false discovery rate. BMC Bioinformatics 7, 123 (2006). [PubMed: 16526949]
78. Thrane AS, Rappold PM, Fujita T, Torres A, Bekar LK, Takano T, Peng W, Wang F, Rangroo Thrane V, Enger R, Haj-Yasein NN, Skare O, Holen T, Klungland A, Ottersen OP, Nedergaard M, Nagelhus EA, Critical role of aquaporin-4 (AQP4) in astrocytic Ca2+ signaling events elicited by cerebral edema. Proceedings of the National Academy of Sciences of the United States of America 108, 846–851 (2011). [PubMed: 21187412]
79. Kang GJ, Ecoiffier T, Truong T, Yuen D, Li G, Lee N, Zhang L, Chen L, Intravital Imaging Reveals Dynamics of Lymphangiogenesis and Valvulogenesis. Scientific reports 6, 19459 (2016). [PubMed: 26785921]
80. Liu HH, Bui BV, Nguyen CT, Kezic JM, Vingrys AJ, He Z, Chronic ocular hypertension induced by circumlimbal suture in rats. Invest Ophthalmol Vis Sci 56, 2811–2820 (2015). [PubMed: 25829414]
81. Gu B, Liu JK, Li XL, Ma QK, Shen MX, Cheng LY, Real-Time Monitoring of Suprachoroidal Space (SCS) Following SCS Injection Using Ultra-High Resolution Optical Coherence Tomography in Guinea Pig Eyes. Invest Ophth Vis Sci 56, 3623–3634 (2015).
82. Peng W, Achariyar TM, Li B, Liao Y, Mestre H, Hitomi E, Regan S, Kasper T, Peng S, Ding F, Benveniste H, Nedergaard M, Deane R, Suppression of glymphatic fluid transport in a mouse model of Alzheimer's disease. Neurobiol Dis 93, 215–225 (2016). [PubMed: 27234656]
83. Zhang C, Lin J, Wei F, Song J, Chen W, Shan L, Xue R, Wang G, Tao J, Zhang G, Xu GY, Wang L, Characterizing the glymphatic influx by utilizing intracisternal infusion of fluorescently conjugated cadaverine. Life sciences 201, 150–160 (2018). [PubMed: 29605446]
84. Wei F, Zhang C, Xue R, Shan LD, Gong S, Wang GQ, Tao J, Xu GY, Zhang GX, Wang LH, The pathway of subarachnoid CSF moving into the spinal parenchyma and the role of astrocytic aquaporin-4 in this process. Life sciences 182, 29–40 (2017). [PubMed: 28576642]

85. Santillan A, Rubin DG, Foley CP, Sondhi D, Crystal RG, Gobin YP, Ballon DJ, Cannulation of the internal carotid artery in mice: a novel technique for intra-arterial delivery of therapeutics. J Neurosci Methods 222, 106–110 (2014). [PubMed: 24269174]

86. Adini I, Ghosh K, Mouse Retinal Whole Mounts and Quantification of Vasculature Protocol. Bio Protoc 5, (2015).

87. Rodriguez AR, Muller LPD, Brecha NC, The RNA binding protein RBPMS is a selective marker of ganglion cells in the mammalian retina. J Comp Neurol 522, 1411–1443 (2014). [PubMed: 24318667]

88. John SW, Hagaman JR, MacTaggart TE, Peng L, Smithes O, Intraocular pressure in inbred mouse strains. Invest Ophthalmol Vis Sci 38, 249–253 (1997). [PubMed: 9008647]

89. Nicholson C, Ion-selective microelectrodes and diffusion measurements as tools to explore the brain cell microenvironment. J Neurosci Methods 48, 199–213 (1993). [PubMed: 8412303]

90. Xu Q, Qaum T, Adamis AP, Sensitive blood-retinal barrier breakdown quantitation using Evans blue. Invest Ophthalmol Vis Sci 42, 789–794 (2001). [PubMed: 11222542]

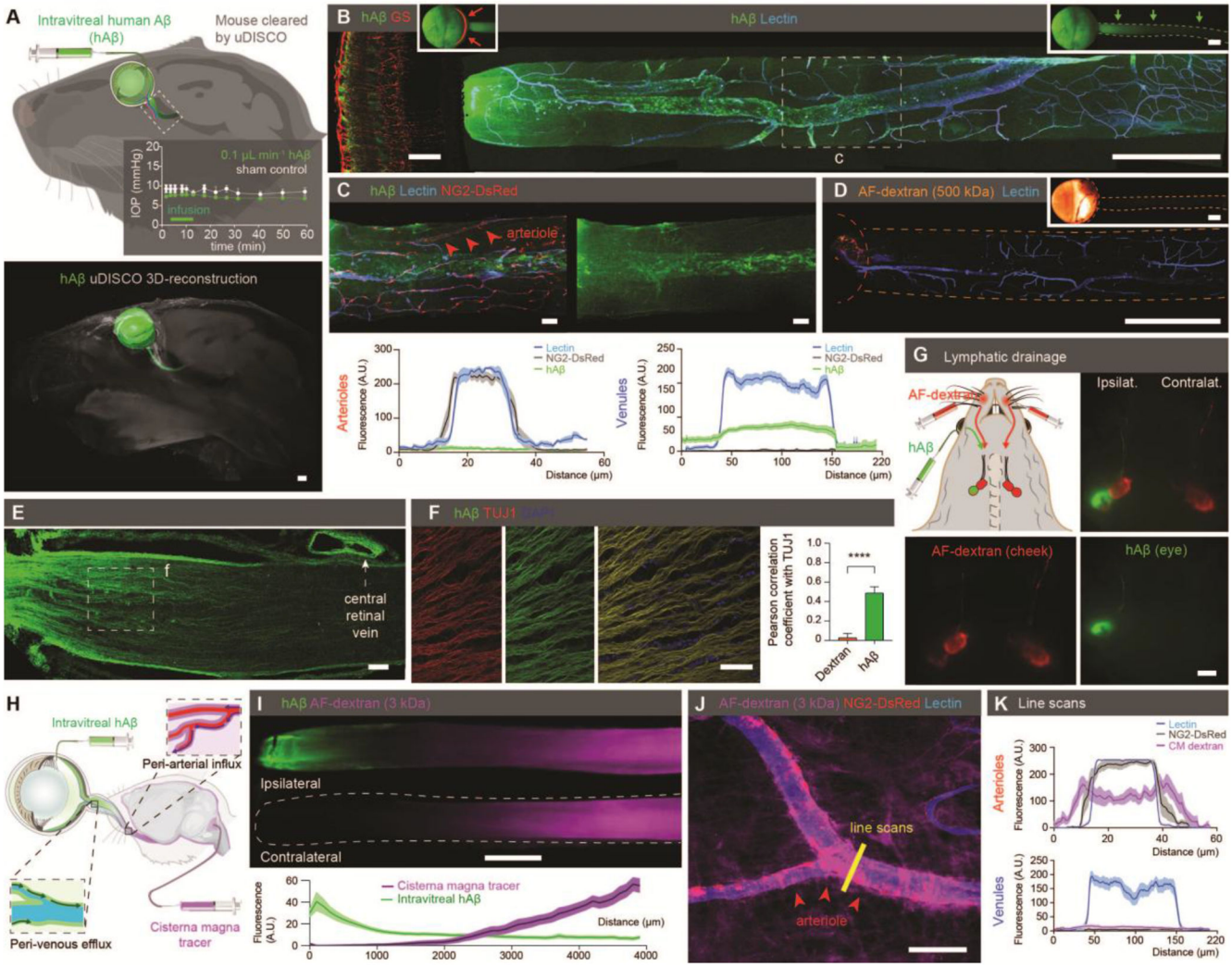

Figure 1. Existence of an ocular glymphatic clearance system.

(**A**) Top: Schematic of intravitreal injection of hAβ. Insert: IOP during injection (n = 5-6, P = 0.0516-0.543, unpaired two-tailed t-test). Rectangle indicates proximal optic nerve displayed in **B-J.** Bottom: uDISCO-cleared transparent mouse heads 1 hour after hAβ injection. (**B**) Confocal images of ipsilateral retina (left) and optic nerve (right) after hAβ intravitreal injection. **B** and **D** inserts display macroscopic images of the eye and optic nerve injected with respective tracers without background subtraction. (**C**) Confocal imaging and quantification of optic nerve from reporter mouse with DsRed-tagged mural cells (vascular smooth muscle cells and pericytes) 30min after intravitreal hAβ injection (mean ± SEM, n = 12-18). (**D**) Confocal image of mouse optic nerve 30min after intravitreal AF-dextran injection. (**E-F**) Confocal imaging and quantification of optic nerve co-labeling with TUJ1 after tracer administration (n = 9-11 ****P < 0.0001 unpaired, two-tailed t-test). Note tracer accumulation in the dural lining of the nerve. (**G**) Cervical lymph nodes exhibiting intense hAβ labeling three hours after injection. (**H**) Schematic of the double injections. (**I**) Representative image and quantification of double injections of hAβ intravitreally and fluorescent tracer intercisternally (mean ± SEM, n = 12). (**J**) Confocal imaging of optic

nerve from reporter mouse with DsRed-tagged mural cells (vascular smooth muscle cells and pericytes) after intracisternal dextran injection with line scan quantified in (K) (mean ± SEM, n = 8-9). (Scales: **A**, **B** right, **D**, **G, I**: 500 μm; **B** left, **C**, **E**, **F**, **J**: 50 μm). A.U., arbitrary units.

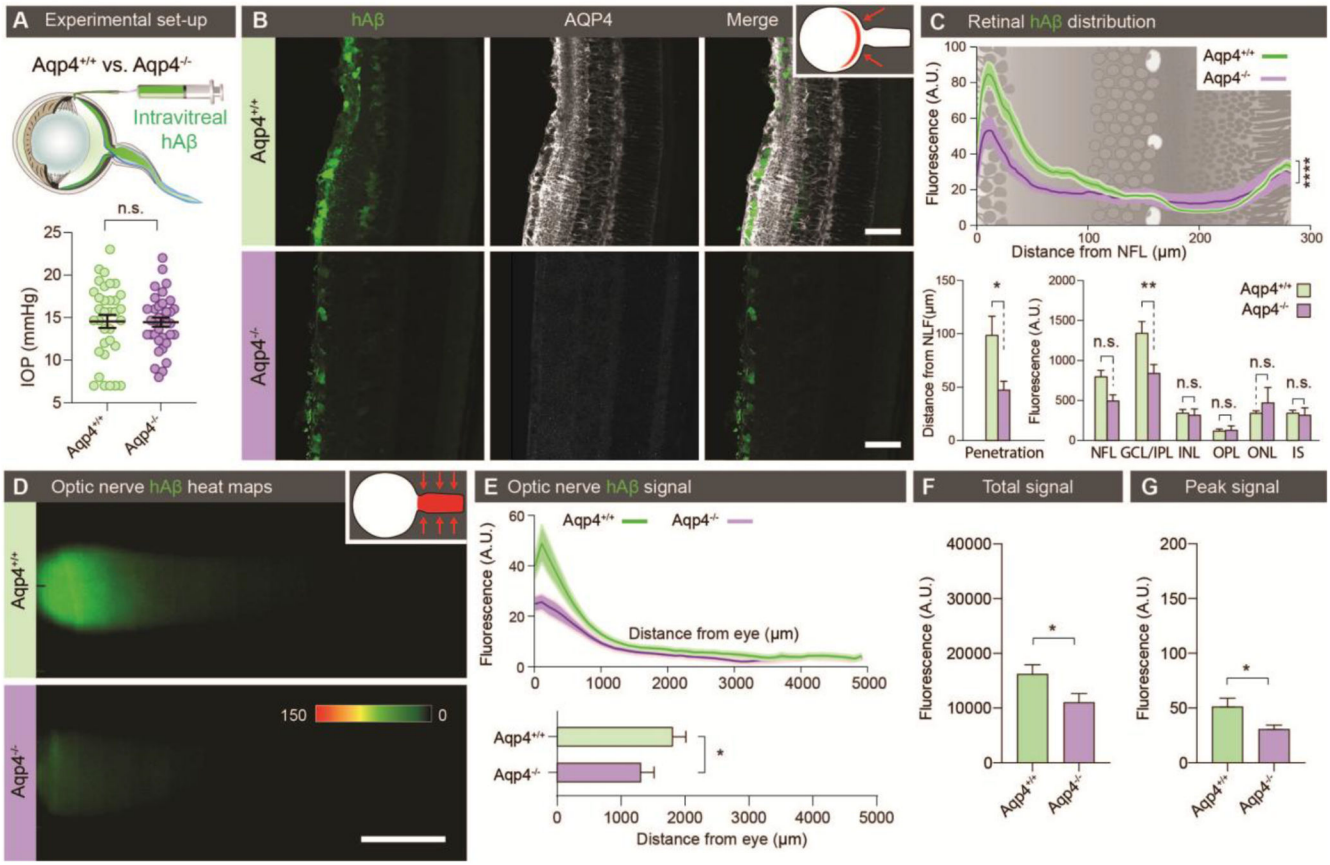

Figure 2. Ocular glymphatic clearance is AQP4-dependent.

(**A**) Top: Experimental setup comparing tracer clearance from the retina and optic nerve after intravitreal injection in *Aqp4*$^{+/+}$ and *Aqp4*$^{-/-}$ mice. Bottom: Scatter plot with mean ± SEM overlaid, comparing intraocular pressure (IOP) in *Aqp4*$^{+/+}$ and *Aqp4*$^{-/-}$ mice before the injection. (**B**) Representative transverse sections of retina collected 30 min after intravitreal hAβ injection and counter-stained for AQP4. (**C**) Line graph overlaid on retinal illustration (top) and bar graphs (bottom) comparing hAβ tracer penetration (n = 7-9, *P < 0.05, Mann-Whitney test) into the various retinal layers (n = 7-9, ** P < 0.01, ****P < 0.0001, two-way ANOVA followed by Sidak's multiple comparisons test).n.s. not significant. (**D**) Representative background-subtracted heat-maps of hAβ signal in the optic nerves of *Aqp4*$^{+/+}$ and *Aqp4*$^{-/-}$ mice 30 min after intravitreal injection. (**E**) Top: Averaged fluorescent intensity profiles of hAβ in the optic nerves from the two groups. Bottom: The distance of tracer transport (n = 23-24 *P < 0.05 Mann-Whitney test). (**F-G**) Total hAβ signal and peak intensity in the optic nerve 30 min after intravitreal injection (n = 23-24, *P < 0.05, unpaired two-tailed t-test for total signal, Mann-Whitney test for peak). (Scales: **B**: 50 μm, **D**: 100 μm).

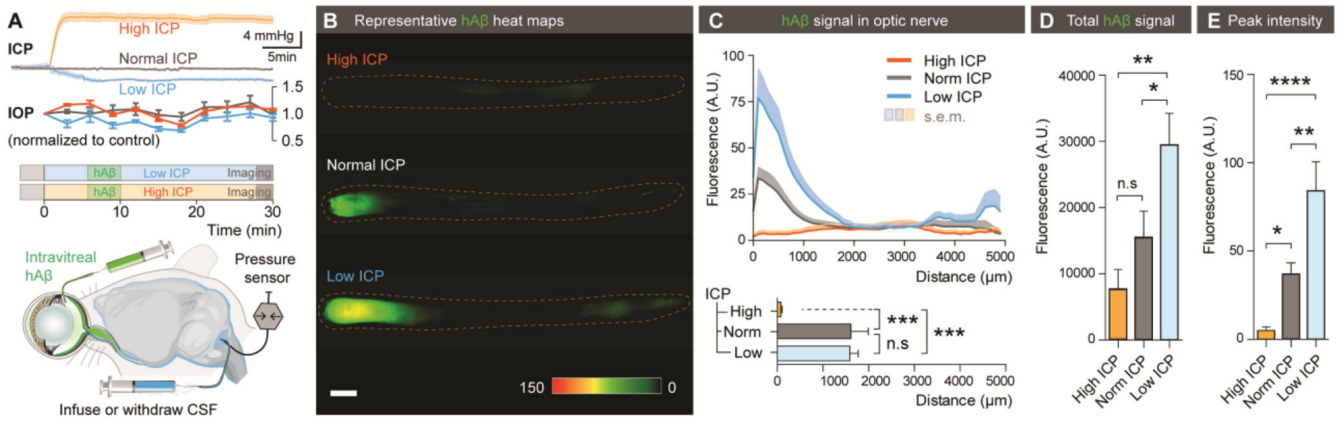

Figure 3. The translaminar pressure difference drives ocular glymphatic outflow.

(**A**) Schematic of the setup used for analyzing hAβ transport following intravitreal injection while manipulating ICP. Top: Mean ICP and IOP normalized to control (± SEM) plotted as a function of time in the high, normal, and low ICP groups (n = 10-12). (**B**) Representative background-subtracted heat-maps of hAβ in the optic nerve from high, normal, and low ICP groups. (**C**) Top: Averaged fluorescent intensity profiles of hAβ in the optic nerves from the three groups. Bottom: The distance of tracer transport (n = 6-8, ***P < 0.001, n.s. P = 0.9976 one-way ANOVA followed by Tukey's *post hoc* test). (**D-E**) Total hAβ signal and peak intensities in the optic nerve 30 min after intravitreal injection (n = 6-8 for each group, *P < 0.05, **P < 0.01, ****P < 0.0001, n.s. P = 0.2996 one-way ANOVA followed by Tukey's *post hoc* test). (Scale: **B**: 500μm).

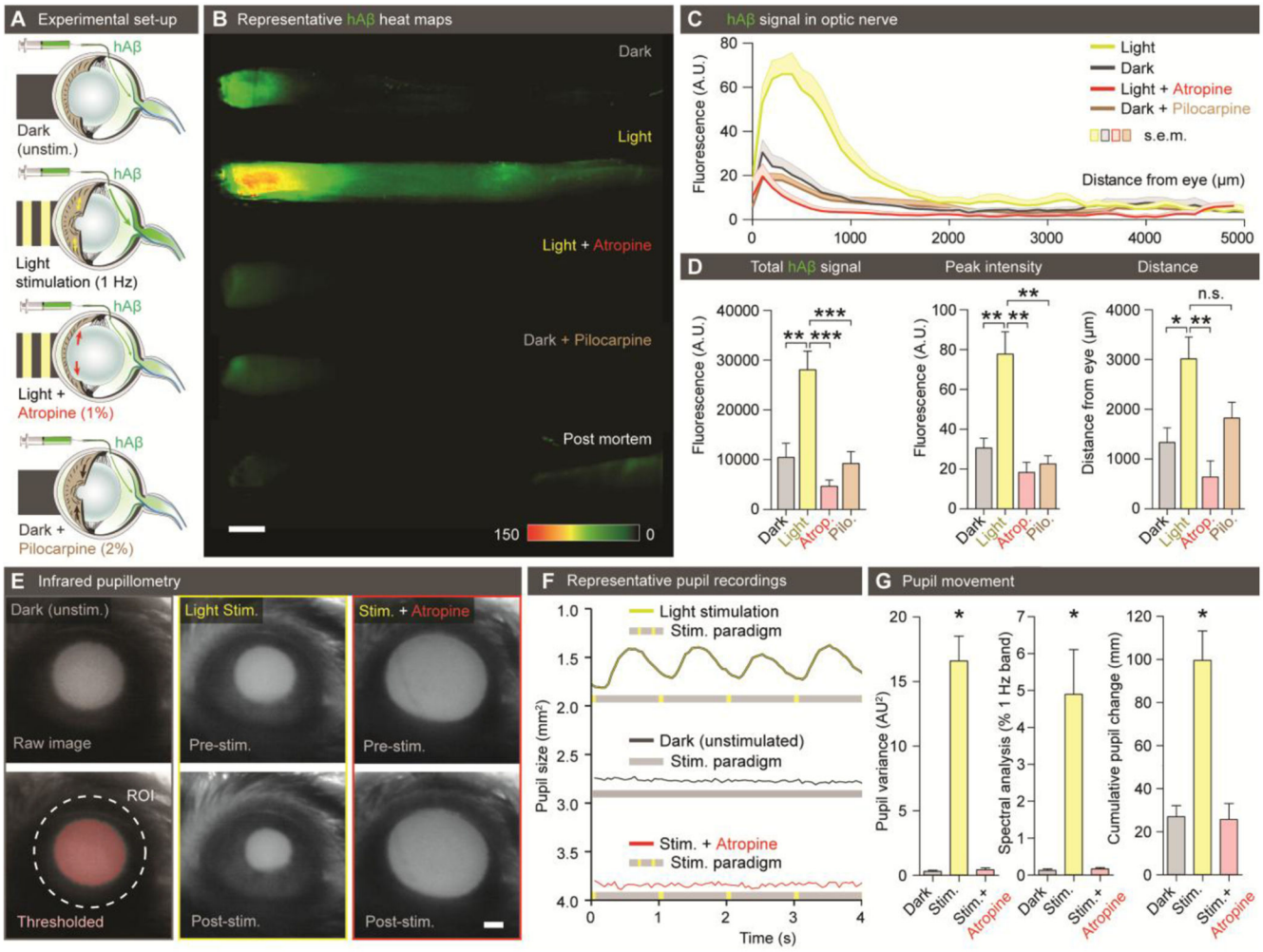

Figure 4. Light stimulation enhances hAβ along the optic nerve.

(**A**) Schematic of the experimental groups. The first group was kept in darkness. The second group was exposed to 1 Hz light-stimulation (100 ms duration, five lumens). The third group was pretreated with atropine (1%) before exposure to 1 Hz light-stimulation. The fourth group was pretreated with pilocarpine (2%) and kept in darkness. (**B**) Representative background-subtracted heat-maps of optic nerves from the four groups 30 min after injection of hAβ and a postmortem group 120 min after injection of hAβ. (**C**) Averaged fluorescent intensity profiles of optic nerves from the four groups (n = 6-19). (**D**) hAβ signal mapped as total signal, peak intensity, and distance of the hAβ transport (n = 6-19, *P < 0.05, **P < 0.01, ***P < 0.001, n.s. P = 0.0756, one-way ANOVA followed by Dunnett's *post hoc* test). (**E**) Infrared pupillometry tracking of the pupil size and light-induced constriction with and without atropine pre-treatment. The pupil area (mm^2) was determined by auto-thresholding. (**F**) Representative pupillometry recordings in dark-exposed and light-stimulated mice with and without atropine administration. (**G**) Left: Comparison of the variance of pupil area in these groups (n = 3, **P < 0.01, one-way ANOVA followed by Dunnett's multiple comparison). Middle: Spectral analysis of pupil response in these groups calculated as % of 1Hz band (n = 3-6, *P < 0.05, One-way ANOVA followed by Dunnett's multiple

comparison). Right: Cumulative pupil diameter change over the time of experiment in these groups (n = 3-6, $*P < 0.05$, Kruskal-Wallis test followed by Dunnett's multiple comparison). (Scale: **B**, **E**: 500μm).

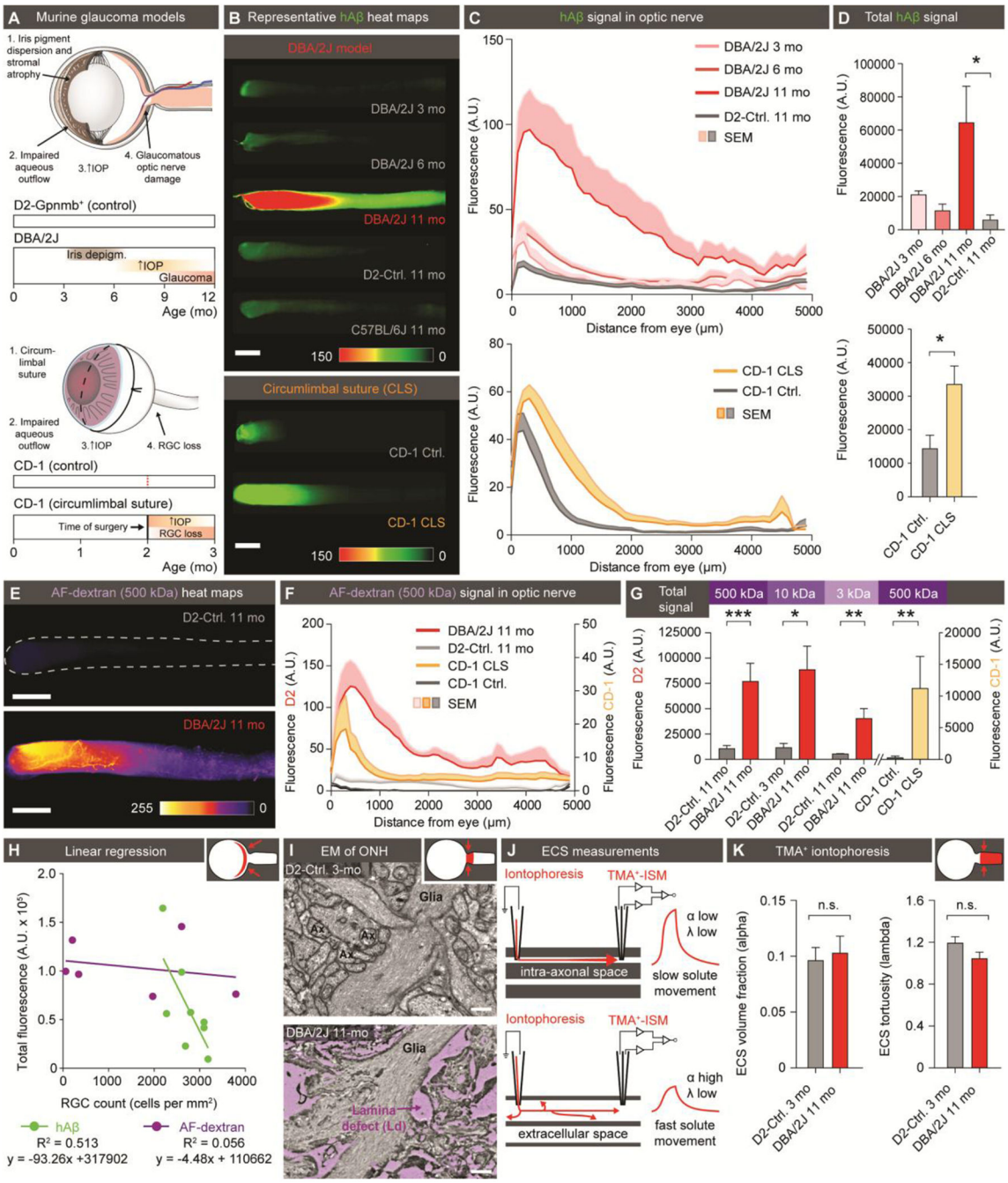

Figure 5. Disruption of the lamina barrier in two distinct murine models of glaucoma reveals a redirection and pathological enhancement of ocular glymphatic outflow.

(**A**) Schematic of disease progression in the DBA/2J strain and chronic CLS model (CD-1) (44, 46). (**B**) Representative background-subtracted heat-maps of optic nerves 30 min after hAβ injection in young, middle-aged, and old DBA/2J mice and old D2-control mice, as well as CD-1-CLS and CD-1-control mice. (**C**) Averaged fluorescent intensity profile of hAβ distribution along the optic nerve in old DBA/2J or CD-1-CLS compared to respective controls (n = 6-11). (**D**) Total hAβ signal in old DBA/2J or CD-1-CLS compared to

respective controls (n = 6-11, *P < 0.05, Kruskal-Wallis followed by Dunn's *post hoc* test for DBA/2J model, unpaired two-tailed t-test for CLS model). (**E**) Representative background-subtracted heat-maps of optic nerves from old DBA/2J and D2-control mice 30 min after intravitreal administration of AF-dextran. (**F**) Averaged fluorescent intensity profile of AF-dextran along the optic nerve in old DBA/2J or CD-1-CLS compared to respective controls (n = 6-9). (**G**) Total signal of different sized AF-dextrans in optic nerve from old DBA/2J or CD-1-CLS compared to respective controls (n = 4-10, *P < 0.05, **P < 0.01, ***P < 0.001, unpaired two-tailed t-test or Mann-Whitney test). (**H**) Total hAβ or AF-dextran signal in the optic nerves of old DBA/2J mice plotted as a function of RGC density in their retinas (n = 6-8). (**I**) Electron micrographs of the glial lamina region from young D2-control and old DBA/2J mice. (**J**) Schematic of real-time TMA^+ iontophoresis measurement. (**K**) TMA^+ measurements of α (extracellular volume space) and λ (extracellular tortuosity) (n = 6-20, P = 0.765 for α, 0.177 for λ, unpaired two-tailed t-test). (Scale: **B**, **E**: 500μm; **I**: 0.5μm).